JGR Oceans

RESEARCH ARTICLE

10.1029/2025JC022493

Anthropogenic Carbon Dynamics: Concentrations, Transports, and Trends in the Western North Atlantic Subtropical Gyre

Daniel Santana-Toscano[1], Peter Brown[2], and Alonso Hernández-Guerra[1]

[1]Unidad Océano y Clima, Instituto de Oceanografía y Cambio Global, IOCAG, Universidad de Las Palmas de Gran Canaria, ULPGC, Unidad Asociada ULPGC-CSIC, Las Palmas de Gran Canaria, Spain, [2]National Oceanography Centre, Southampton, UK

Key Points:

- Anthropogenic carbon transport in the western North Atlantic is driven by ocean circulation and rising carbon concentrations
- Surface and intermediate water masses show the greatest increases in carbon transport, with minimal variability in deeper layers
- Regional currents influence spatial variability in carbon distribution

Correspondence to:

D. Santana-Toscano,
daniel.santana@ulpgc.es

Citation:

Santana-Toscano, D., Brown, P., & Hernández-Guerra, A. (2025). Anthropogenic carbon dynamics: Concentrations, transports, and trends in the western North Atlantic Subtropical Gyre. *Journal of Geophysical Research: Oceans*, *130*, e2025JC022493. https://doi.org/10.1029/2025JC022493

Received 13 FEB 2025
Accepted 15 JUN 2025

Author Contributions:

Conceptualization: Alonso Hernández-Guerra
Data curation: Daniel Santana-Toscano
Formal analysis: Daniel Santana-Toscano, Peter Brown, Alonso Hernández-Guerra
Funding acquisition: Alonso Hernández-Guerra
Investigation: Daniel Santana-Toscano, Peter Brown, Alonso Hernández-Guerra
Methodology: Daniel Santana-Toscano, Alonso Hernández-Guerra
Project administration: Alonso Hernández-Guerra
Supervision: Peter Brown, Alonso Hernández-Guerra
Validation: Daniel Santana-Toscano, Alonso Hernández-Guerra
Visualization: Daniel Santana-Toscano, Peter Brown
Writing – original draft: Daniel Santana-Toscano

Abstract The ocean acts as a major carbon sink, absorbing anthropogenic CO_2 and mitigating climate change. The North Atlantic Ocean, particularly the western North Atlantic Subtropical Gyre (NASG), plays a crucial role in this process, yet the mechanisms governing the transport of anthropogenic carbon (C_{anth}) remain incompletely understood. In this study, we quantify C_{anth} transport across the western NASG using hydrographic observations from repeat meridional sections (A20 and A22) and an inverse box model approach. We show that C_{anth} transport has increased over the past four decades, primarily in surface and intermediate layers, driven by rising atmospheric CO_2 concentrations rather than significant changes in mass transport. The strongest C_{anth} transport occurs in the Subtropical Underwater (STUW) and Subtropical Mode Water (STMW) layers, following the circulation patterns of the Gulf Stream (GS) and its recirculation. While deep and bottom layers, such as Labrador Sea Water, Iceland-Scotland Overflow Water, and Denmark Strait Overflow Water, exhibit weaker and more variable transport, the overall trend reflects increasing C_{anth} sequestration across the region. Long-term atmospheric CO_2 trends from four global monitoring stations are compared with C_{anth} levels in the western NASG, showing that both have steadily increased since 1970. Slight variations in these trends imply that factors such as ocean circulation, temperature fluctuations, and water mass dynamics could affect the region's efficiency in CO_2 uptake.

Plain Language Summary This study looks at how the western North Atlantic Ocean absorbs extra carbon dioxide from the atmosphere—a process that helps fight climate change. Researchers found that over the past 40 years, more carbon dioxide has been entering the ocean, especially in the upper and middle layers. This increase is mostly due to rising levels of carbon dioxide in the atmosphere, not because the water itself is moving any differently. The strongest uptake happens in water layers that follow the Gulf Stream's path. Although deeper layers show less consistent behavior, the overall trend is clear: the region is locking away more carbon dioxide over time. This pattern matches global trends since 1970, though factors such as ocean currents, temperature changes, and the mixing of different water masses can also affect how well the ocean captures carbon dioxide.

1. Introduction

The ocean serves as a vital regulator of Earth's climate by absorbing nearly one-fourth of the CO_2 released into the atmosphere through human activities such as fossil fuel burning and land-use changes (Friedlingstein et al., 2023; Gruber et al., 2019; Khatiwala et al., 2009). This process mitigates the effects of anthropogenic emissions but simultaneously drives significant changes in the marine carbonate system, such as reductions in pH and carbonate ion concentrations ($[CO_3^{2-}]$; Doney et al., 2020; Gattuso et al., 2015). These changes, collectively termed Ocean Acidification (OA), reflect the imbalance created by increasing atmospheric CO_2 levels and have wide-ranging implications for marine ecosystems, biogeochemical cycles, and global climate regulation (Caldeira & Wickett, 2003, 2005; Doney et al., 2009; Orr et al., 2005; Raven et al., 2005). Understanding the ocean's role as a carbon sink, particularly in regions with intense CO_2 uptake such as the North Atlantic Ocean, is crucial for predicting the future trajectory of global carbon dynamics (Asselot et al., 2024; Curbelo-Hernández et al., 2024).

The North Atlantic Ocean is recognized as one of the strongest oceanic CO_2 sinks, storing approximately 23%–38% of the global anthropogenic carbon (C_{anth}) inventory (Khatiwala et al., 2013; Sabine et al., 2004). This phenomenon is driven by two key mechanisms: the efficient absorption of atmospheric CO_2 in subtropical North

Writing – review & editing: Daniel Santana-Toscano, Alonso Hernández-Guerra

Atlantic surface waters, aided by low Revelle factors -which is the ratio of the fractional change in seawater CO_2's partial pressure to the fractional change in dissolved inorganic carbon-, and the subsequent poleward transport of these carbon-enriched waters (Brown et al., 2021; Pérez et al., 2013; Sabine et al., 2004). Deep-water formation processes in the subpolar North Atlantic then facilitate the subduction of C_{anth} into the ocean, ensuring its long-term storage (Pérez et al., 2010; Sabine et al., 2004). This intricate interplay between surface uptake, transport, and deep storage positions the North Atlantic as a critical player in the global carbon cycle (Gruber et al., 2019).

Within this larger system, the western North Atlantic Subtropical Gyre (NASG) emerges as a region of particular interest. Characterized by high CO_2 fluxes driven by air-sea disequilibria, this region experiences significant seasonal and interannual variability in C_{anth} uptake (Bonou et al., 2024). Seasonal temperature fluctuations dominate the variability in CO_2 solubility while biological processes such as photosynthesis and remineralization further modulate the carbon dynamics (Gruber et al., 2019; Raven et al., 2005). Additionally, physical processes such as the strength and variability of the Atlantic Meridional Overturning Circulation (AMOC), along with climatic drivers such as the North Atlantic Oscillation (NAO), exert a strong influence on C_{anth} distribution and storage (García-Ibáñez et al., 2016; Pérez et al., 2018). Changes in these processes, whether through natural variability or anthropogenic forcing, can significantly alter the region's capacity to act as a carbon sink (Pérez et al., 2013).

The long-term accumulation of C_{anth} in the ocean has consequences beyond the uptake of atmospheric CO_2. This accumulation alters the carbonate chemistry of seawater, increasing the Revelle factor and reducing the buffering capacity of the ocean, thereby making the ocean more sensitive to further CO_2 increases (Caldeira & Wickett, 2003). In the western NASG, this process is of particular concern, as changes in oceanic circulation patterns, deep-water formation, and surface warming could diminish the region's ability to sequester carbon over time. Furthermore, the impacts of OA, such as the shoaling of the aragonite saturation horizon and the subsequent exposure of sensitive marine ecosystems to undersaturated conditions, underscore the urgency of understanding the dynamics of C_{anth} in this region (Feely et al., 2004; Guinotte et al., 2006).

While significant progress has been made in studying the North Atlantic, particularly regarding C_{anth} concentrations and uptake dynamics, there is still much to uncover about the mechanisms governing C_{anth} transport within the region (Caínzos et al., 2022). Emerging technologies, such as BGC-Argo floats and neural network-based estimation methods, are revolutionizing the study of C_{anth} by providing unprecedented opportunities to examine its fine-scale distribution, temporal evolution, and transport (Asselot et al., 2024). However, traditional methods, including ship-based measurements of the carbonate system and transient tracers such as chlorofluorocarbons (CFCs), remain foundational in this work. These methods offer robust high-quality data essential for understanding C_{anth} dynamics and serve as critical benchmarks for validating and complementing data from modern technologies (Talley et al., 2016). Together, these approaches enable a more comprehensive understanding of C_{anth} variability and transport processes. Understanding the pathways and rates at which C_{anth} is redistributed through ocean circulation and vertical mixing processes (García-Ibáñez et al., 2016; Pérez et al., 2018) requires a shift from a concentration-centric approach to a transport-focused perspective. Such a shift would provide crucial insights into how atmospheric CO_2 uptake integrates with regional circulation features, including the AMOC, and its impact on long-term carbon storage. Addressing these gaps is essential for fully understanding the western NASG's role in the global carbon cycle and its response to ongoing climate change (Bonou et al., 2024; Doney et al., 2020; Friedlingstein et al., 2023; Li et al., 2024).

This study focuses on the western NASG, aiming to advance our understanding of the mechanisms governing the transport of C_{anth} within this region. By examining the pathways of C_{anth} redistribution through ocean circulation and the influence of regional dynamics such as the Gulf Stream (GS), the Deep Western Boundary Current (DWBC), and regional currents, we seek to provide a more comprehensive view of its role in the carbon cycle. Through the integration of hydrographic observational data and the inverse modeling approach, this work emphasizes the importance of transport processes in shaping C_{anth} variability. These findings are expected to enhance predictions of how changes in circulation and atmospheric CO_2 levels will influence C_{anth} transport, ultimately contributing to strategies for mitigating the impacts of climate change.

This paper is organized as follows: Section 2 provides an overview of the hydrographic and atmospheric data utilized in this study, including the geostrophic velocity calculations, the setup of the inverse box model, and the methods used to estimate C_{anth}. Section 3 explores the temporal and spatial evolution of C_{anth} concentration and transport across water masses, latitudes, and time. It also identifies the primary drivers behind the increasing C_{anth}

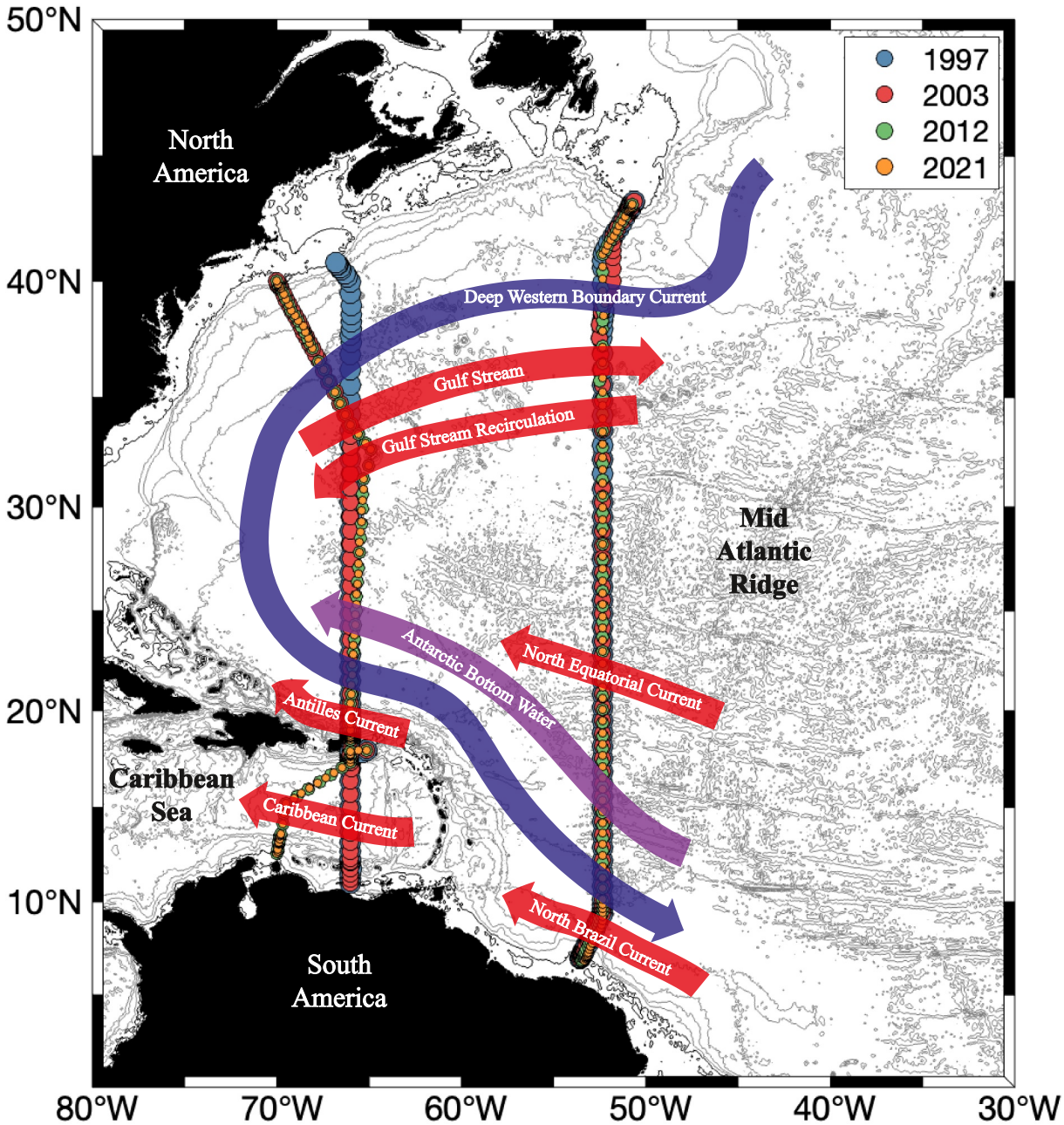

Figure 1. Map of the hydrographic sections defining the boundaries of the inverse box model. The A20 section is positioned nominally at 52°W while the A22 section lies at 66°W. Stations sampled during the 1997, 2003, 2012, and 2021 surveys are represented by blue, red, green, and orange dots, respectively, for each section. Surface currents are shown in red, deep currents in dark blue, and bottom currents in purple, following the circulation scheme of Santana-Toscano et al. (2025).

transport in the western NASG and examines the relationship between atmospheric CO_2 concentrations and oceanic C_{anth} concentrations. Finally, Section 4 contextualizes the findings within the framework of recent advancements in understanding C_{anth} dynamics across the tropical, subtropical, and subpolar North Atlantic Ocean.

2. Data and Methods

2.1. Hydrographic Data

This study analyzes hydrographic data collected from two meridional sections, A20 (52°W) and A22 (66°W), located in the western NASG (Figure 1). These sections were sampled as part of repeat hydrography surveys

conducted in 1997, 2003, 2012, and 2021. Each section intersects key oceanographic features, including major currents such as the GS, the DWBC, the North Brazil Current (NBC), and the North Equatorial Current (NEC). These currents play a critical role in the transport and redistribution of heat, freshwater, and biogeochemical properties across the region, making these sections ideal for studying variability in ocean circulation and C_{anth} transport (Casanova-Masjoan et al., 2018; Joyce et al., 2001; Santana-Toscano et al., 2023, 2025). For this study, we utilized 77, 82, 81, and 90 high-quality stations from the A22 section in 1997, 2003, 2012, and 2021, respectively, and 95, 88, 83, and 90 high-quality stations from the A20 section for the same years. Sampling for both sections was conducted during boreal summer in 1997, boreal fall in 2003, and boreal spring in 2012 and 2021.

The hydrographic data were collected as part of the Global Ocean Ship-Based Hydrographic Investigations Program (GO-SHIP) and are publicly available through the CLIVAR and Carbon Hydrographic Data Office (CCHDO) and through the Global Ocean Data Analysis Project (GLODAP). The data sets include measurements of temperature, salinity, dissolved oxygen, and a suite of biogeochemical variables, such as total alkalinity (AT), dissolved inorganic carbon (CT), and nutrients (nitrate, phosphate, silicate). Additionally, SADCP velocities are recorded by an instrument mounted on the hull of the moving vessel, providing continuous measurements along the ship's track. In contrast, LADCP velocities are obtained from an ADCP package attached to the rosette and lowered through the water column, yielding high-vertical-resolution snapshots at discrete station locations. To facilitate analysis, variables were interpolated onto a uniform grid using a neutral density framework (γ^n; Jackett & McDougall, 1997). This approach aligns water properties along isopycnal surfaces, which better represent the continuity of water masses compared to depth levels. Interpolation was performed every 2 dbar, consistent with the vertical resolution of the CTD casts, using a 2D linear interpolation with Delaunay triangulation for scattered data and nearest extrapolation for missing values.

2.2. Atmospheric Data

Wind velocity data used to estimate Ekman transport were obtained from the National Center for Environmental Prediction Reanalysis II (NCEP-DOE) project, provided by the National Oceanic and Atmospheric Administration (NOAA; Kanamitsu et al., 2002). The hourly data were averaged over the duration of each cruise and calculated at a height of 10 m above sea level. The data set spanned the area between each section and the American coastline, with a spatial resolution of $2.5° \times 2.5°$, while maintaining the same latitudinal boundaries as the cruises.

The data on atmospheric CO_2 concentrations used in this study were retrieved from the NOAA Global Monitoring Laboratory (GML) Carbon Cycle Greenhouse Gases (CCGG) database. This data set provides hourly, daily, and monthly averages of atmospheric CO_2 dry air mole fractions, based on quasi-continuous measurements from multiple locations, including Barrow (Alaska), Mauna Loa (Hawaii), American Samoa, and the South Pole, spanning from 1973 to the present (Thoning et al., 2024).

2.3. Geostrophy and Inverse Model

To calculate the geostrophic velocity between station pairs, we employed the thermal wind equation (Cushman-Roisin & Beckers, 1994). In this process, we assumed a level of no motion—setting the reference velocity to zero—between the two counter-flowing water masses (NADW and AABW; Table 1; Casanova-Masjoan et al., 2018; Joyce et al., 2001; Santana-Toscano et al., 2023). Specifically, this level corresponds to the neutral density interface at $\gamma^n = 28.14$ kg m^{-3}. For station pairs where the seafloor is shallower than this reference level, the closest common depth was used as the reference. The relative geostrophic velocity was then adjusted using ADCP measurements, following the methodology outlined by Comas-Rodríguez et al. (2010) and Santana-Toscano et al. (2023). This adjustment involved visually comparing the vertical profiles of geostrophic velocities, mean SADCP velocities between station pairs, and mean LADCP velocities for each station. When the ADCP velocity profiles aligned with the geostrophic velocities, an adjustment was performed over a selected depth interval where they matched. The geostrophic velocity was corrected by adding the average difference -computed over the selected depth range-between it and the chosen ADCP velocity. However, not all station pairs underwent adjustment due to inconsistencies in the shear between ADCP and geostrophic velocity profiles, leaving some geostrophic velocities unadjusted.

Table 1
Neutral Density Limits for Each Layer and Their Associated Water Masses With the Level of No Motion Highlighted in Bold

Layer	Neutral density (γ^n) range	Water mass
1	$\gamma^n < 26.4$	North Atlantic Subtropical Underwater (STUW)
2	$26.4 < \gamma^n < 26.6$	Subtropical Mode Water (STMW)
3	$26.6 < \gamma^n < 27$	Antarctic Intermediate Water (AAIW)
4	$27 < \gamma^n < 27.5$	
5	$27.5 < \gamma^n < 27.7$	
6	$27.7 < \gamma^n < 27.8$	
7	$27.8 < \gamma^n < 27.875$	Labrador Sea Water (LSW)
8	$27.875 < \gamma^n < 27.925$	
9	$27.925 < \gamma^n < 27.975$	
10	$27.975 < \gamma^n < 28$	Iceland-Scotland Overflow Water (ISOW)
11	$28 < \gamma^n < 28.05$	
12	$28.05 < \gamma^n < 28.1$	Denmark Strait Overflow Water (DSOW)
13	$28.1 < \gamma^n <$ **28.14**	
14	**28.14** $< \gamma^n <$ bot.	Antarctic Bottom Water (AABW)

The initial geostrophic estimation of velocity for each station pair is computed assuming a null velocity at a reference level. However, this level of no motion has a velocity different from zero. Inverse models are used to estimate reference-level velocities for each station pair by applying mass conservation constraints as equations in a matrix form (Ganachaud & Wunsch, 2000; Hernández-Guerra et al., 2019; Wunsch, 1978, 1996):

$$Ab + n = -Y$$

where A is a matrix containing the mass of each layer at station pairs, b is a vector of unknown reference velocities and adjustments to Ekman transport, n is the noise vector, and Y is a vector representing mass transport imbalances in each layer from the relative velocity field. The combination of mass conservation equations and their associated uncertainties forms an underdetermined system, which can be solved using the Gauss-Markov estimator. This method provides an estimate that minimizes the error with the real value based on initial and noise information. Additionally, it quantifies uncertainties in the solution (Wunsch, 1996).

A single-box inverse model was applied independently to each section, A20 and A22, and for each of the years surveyed. This approach has been widely used in previous studies (Arumí-Planas et al., 2023; Caínzos et al., 2023; Casanova-Masjoan et al., 2018; Hall, 2004; Joyce et al., 2001; Santana-Toscano et al., 2023). The single-box models consist of 14 mass conservation equations, corresponding to 14 neutral density layers spanning the water column (Table 1). Additionally, an overall mass conservation equation was included for the entire water column. Unknowns in the inverse model were solved using the Gauss-Markov method, minimizing error variances while requiring a priori variances for both velocities and equations. Following Santana-Toscano et al., 2025, a priori velocity variances of $(0.03\ \text{m s}^{-1})^2$ were used for station pairs with ADCP adjustments, and higher variances of $(0.06\ \text{m s}^{-1})^2$ were applied to unadjusted pairs. A priori equation variances were set at $(2\ \text{Sv})^2$ for surface layers and $(1\ \text{Sv})^2$ for deeper layers and overall mass conservation.

2.4. C_{anth} Estimations

The concentration of C_{anth} cannot be directly measured in the ocean and is instead inferred from other water sample parameters using methods that assume a steady-state ocean. Among these methods, back-calculation techniques are widely employed. These include ΔC^* (Gruber et al., 1996), the TrOCA method—which combines oxygen, inorganic carbon, and total alkalinity (Touratier et al., 2007)—and φC_T^0 (Pérez et al., 2008; Vázquez-Rodríguez et al., 2009). Additionally, approaches based on transit time distributions are also commonly used (Waugh et al., 2006). Here, the φC_T^0 back-calculation method is used to estimate the preformed dissolved inorganic carbon concentration of a water sample when it last interacted with the surface. This method uses

variables such as total alkalinity (AT), oxygen utilization, salinity, and temperature while accounting for temporal variations in CO_2 air-sea disequilibrium. Its ability to handle regions with strong mixing processes makes it an improvement over the ΔC* method (Caínzos et al., 2022; Matear et al., 2003; Thomas & Ittekkot, 2001). The uncertainty of C_{anth} estimates made with the φC_T^0 method is ±5.2 μmol kg^{-1} (Vázquez-Rodríguez et al., 2009).

The transport of C_{anth} was evaluated across the western NASG by combining biogeochemical data with geostrophic velocity estimates derived from inverse models. The transport of any property (T) is calculated for each pair of consecutive hydrographic stations and between two neutral density interphases using the following equation:

$$T = \iint C\rho v dy d\gamma^n$$

where C represents the concentration of the property, ρ is the in situ density, v is the geostrophic velocity from the inverse model perpendicular to the section, and $dyd\gamma^n$ refers to the area over which the computation is performed, taking into account the distance between stations and the width of each vertical layer, respectively.

3. Results

Over the 24-year span encompassing the 1997, 2003, 2012, and 2021 surveys, both the A20 (52°W) and A22 (66°W) transects record a systematic rise in C_{anth} concentrations throughout the water column. In 1997, waters from 0 to 750 m held roughly 30–50 μmol kg^{-1}, AAIW averaged 5–10 μmol kg^{-1}, and deeper layers registered 5–10 μmol kg^{-1}. By 2003, surface values climbed to 40–70 μmol kg^{-1}, AAIW stayed similar to 1997, and deep-water concentrations rose in the northern part of the two sections to 10–15 μmol kg^{-1}. The 2012 sections show further growth—surface waters reached 60–80 μmol kg^{-1}, AAIW averaged 15–20 μmol kg^{-1}, and deep masses were in the range of 10–15 μmol kg^{-1}. The 2021 survey captures peak surface C_{anth} concentrations of 70–100 μmol kg^{-1}, intermediate levels of 20–25 μmol kg^{-1}, and deep-water concentrations reaching 15–20 μmol kg^{-1}.

The analysis illustrates C_{anth} transport (kmol/s) by water mass in two sections—A20 (Figures 3a and 3b) and A22 (Figures 3c and 3d)—each highlighting distinct regional dynamics. Eastward fluxes are indicated by positive zonal transport values while westward fluxes are represented by negative ones. In the portions of both sections located below 28°N (Figures 3a and 3d), the transport in the surface and intermediate layers is mostly westward. This behavior is driven by currents such as the NBC, NEC, and the Antilles Current (Casanova-Masjoan et al., 2018; Santana-Toscano et al., 2023). In contrast, in the regions above 28ºN (Figures 3b and 3e), the surface and intermediate layers exhibit a predominantly eastward C_{anth} transport. Here, the GS plays a dominant role, contributing with significantly higher net transport due to its stronger intensity when compared with the westward currents (Santana-Toscano et al., 2023). A dedicated focus on the Caribbean Sea within the A22 section (Figure 3c) reveals that the C_{anth} transport in this region mirrors the characteristic westward mass flux typically observed there (Casanova-Masjoan et al., 2018; Joyce et al., 2001). Across all segments, the deep and bottom layers show much weaker C_{anth} transport than the surface and intermediate layers—a finding that aligns with the generally lower C_{anth} concentrations found at depth. Nevertheless, features such as the DWBC are noticeable; there is a slight eastward transport in the deep layers below 28°N and a slight westward transport in the deep layers above 28°N. Despite the seasonal variability observed over the surveyed years (with indicators for 1997, 2003, 2012, and 2021), an overall increasing trend in the surface and intermediate layers is apparent.

The northward-accumulated C_{anth} transport along the A20 (Figures 4a–4g) and A22 (Figures 4h–4n) sections closely follows the regional mass-transport distribution (Casanova-Masjoan et al., 2018; Santana-Toscano et al., 2023). The STUW and STMW layers carry the largest C_{anth} loads, with transport veering steadily westward from the southernmost latitudes up to 33°N (Figures 4a, 4b, 4h, and 4i). There, the slope steepens sharply, marking the GSR, and beyond 37.5°N a persistent eastward jet—the GS itself—sustains high C_{anth} transport toward the northern boundary (Casanova-Masjoan et al., 2018; Santana-Toscano et al., 2023). Intermediate layers such as AAIW and Labrador Sea Water (LSW) (Figures 4c, 4d, 4j, and 4k) exhibit more variable profiles: modest eastward transport at lower latitudes transitions through the GSR and GS signatures. In deeper layers, Iceland-Scotland Overflow Water (ISOW) shows almost no C_{anth} signal, whereas Denmark Strait Overflow Water

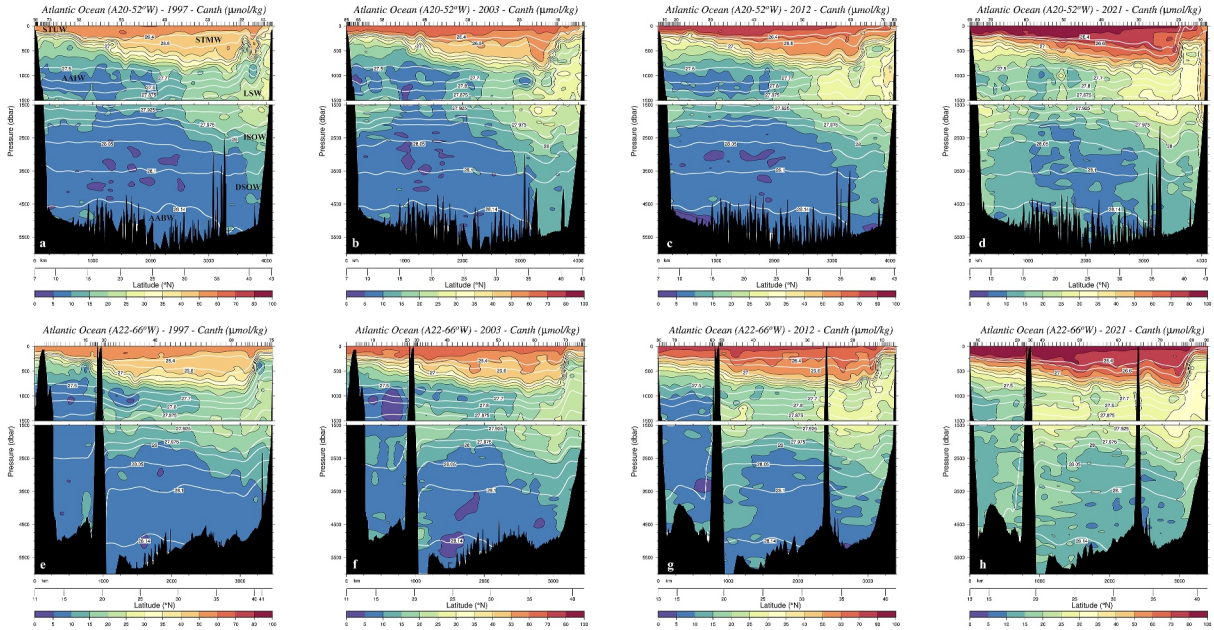

Figure 2. Vertical sections of C_{anth} concentration (µmol/kg) at A20 (52°W; a–d) and A22 (66°W; e–h) with neutral density (γ^n, kg m^{-3}) shown as white contour. STMW, Subtropical Mode Water; STUW, Subtropical Underwater; AAIW, Antarctic Intermediate Water; LSW, Labrador Sea Water; ISOW, Iceland-Scotland Overflow Water; DSOW, Denmark Strait Overflow Water; AABW, Antarctic Bottom Water.

(DSOW) echoes the alternating eastward–westward pattern seen above, albeit inconsistently across survey years. AABW contributes the least, with transport values remaining near zero in most cases.

A clear net increase in C_{anth} transport over time emerges from the survey data (Figures 3 and 4). To untangle the contributions of rising C_{anth} concentrations versus changes in mass transport, we applied a linear regression between C_{anth} transport and mass transport and quantified its slope for each water mass in the A22 (Figure 5a) and A20 (Figure 5b) sections. Surface and intermediate layers show the strongest growth: STUW transport climbed from ∼50 to ∼75 µmol kg^{-1} and STMW from ∼28 to ∼43 µmol kg^{-1} between 1997 and 2021 (Figures 5a and 5b). For deeper water masses, signals were separated into northern and southern regions, as these masses are not present throughout the entire basin, and including all latitudes would underrepresent regional differences. Both northern and southern LSW exhibit steady increases across A22 and A20, whereas ISOW and DSOW display greater interannual variability—particularly in A22—but consistently higher northern growth rates. Across all water masses, the persistence of these positive slopes confirms that the observed intensification of C_{anth} transport is driven predominantly by rising concentrations rather than by changes in mass transport (Figure 5).

After identifying the increase in C_{anth} concentration as the primary driver of the rise in C_{anth} transport over the years in the western NASG, a critical question arises: is the western NASG, along with the surrounding areas, absorbing CO_2 from the atmosphere at a rate sufficient to keep up with the rapid increase in atmospheric CO_2? To explore this, we examined the temporal trends of atmospheric CO_2 concentrations at four key monitoring stations —Barrow, Alaska (BRW); Mauna Loa, Hawaii (MLO); American Samoa (SMO); and the South Pole (SPO)—as well as the mean atmospheric CO_2 concentration derived from these stations. Figure 6 presents these trends, alongside the temporal trends of mean oceanic C_{anth} concentrations observed in the A20 and A22 sections during the surveyed years. The individual monitoring stations exhibit a consistent upward trajectory in atmospheric CO_2 from 1970 to 2025 (Figures 6a–6d). Despite geographic differences, the trends across stations are remarkably similar, indicating a globally uniform increase in atmospheric CO_2 concentrations over time. The mean oceanic C_{anth} concentration in the A20 and A22 sections closely mirrors the upward trend of atmospheric CO_2 (Figure 6e). While the fitted trends for both atmospheric CO_2 and oceanic C_{anth} concentrations are similar, subtle differences may suggest variability in the region's ability to absorb atmospheric CO_2. According to Müller et al. (2023), this

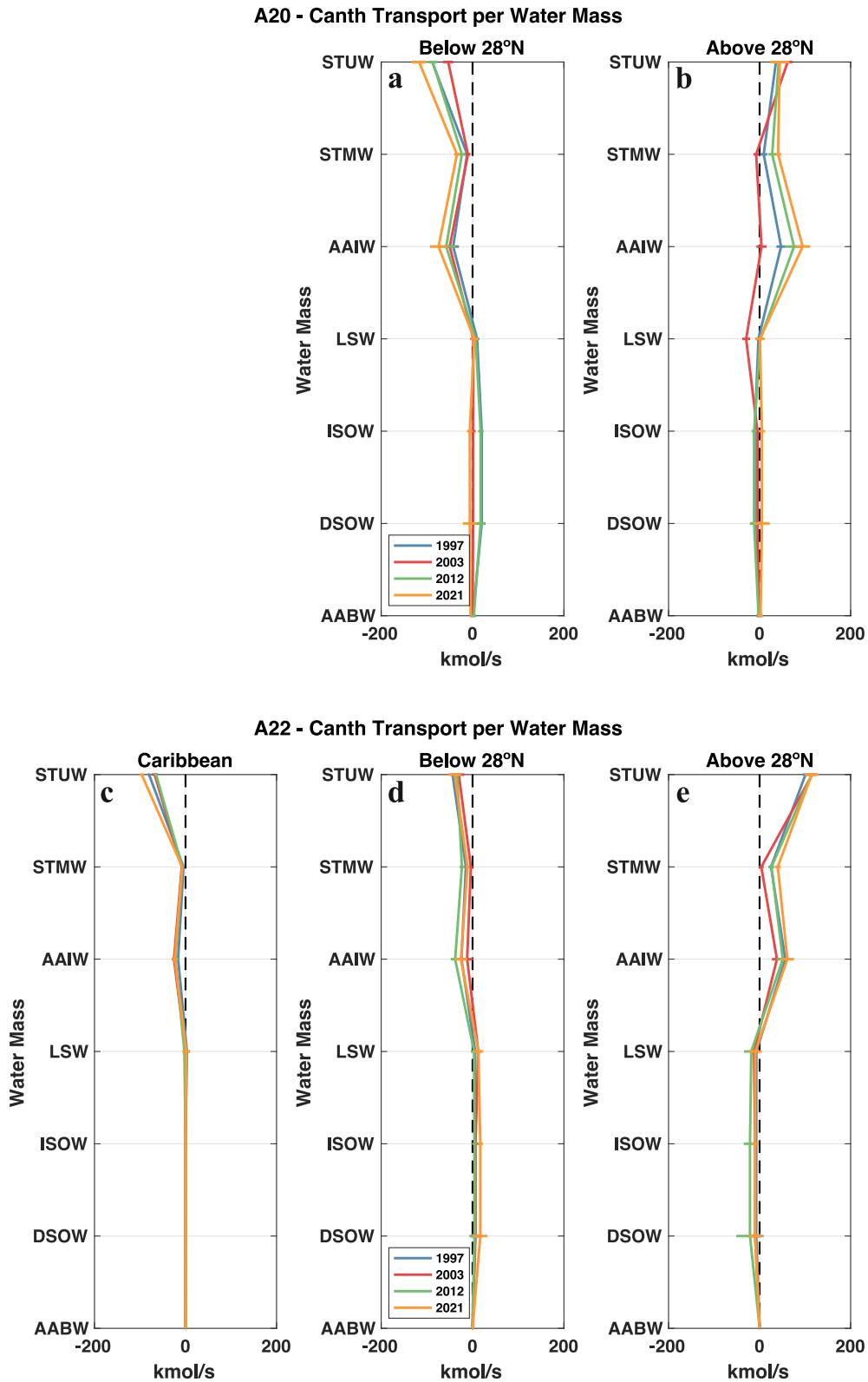

Figure 3. Vertical distribution of C_{anth} transport (kmol/s) by water mass and year, with 1997, 2003, 2012, and 2021 represented by blue, red, green, and orange lines, respectively. Panels (a and b) show the A20 section (52°W) while panels c to e depict the A22 section (66°W). The figure highlights three distinct dynamical regions within the western NASG: the Caribbean Sea (c), the southern regions (a, c), and the northern regions (b, e), separated by the 28°N latitude.

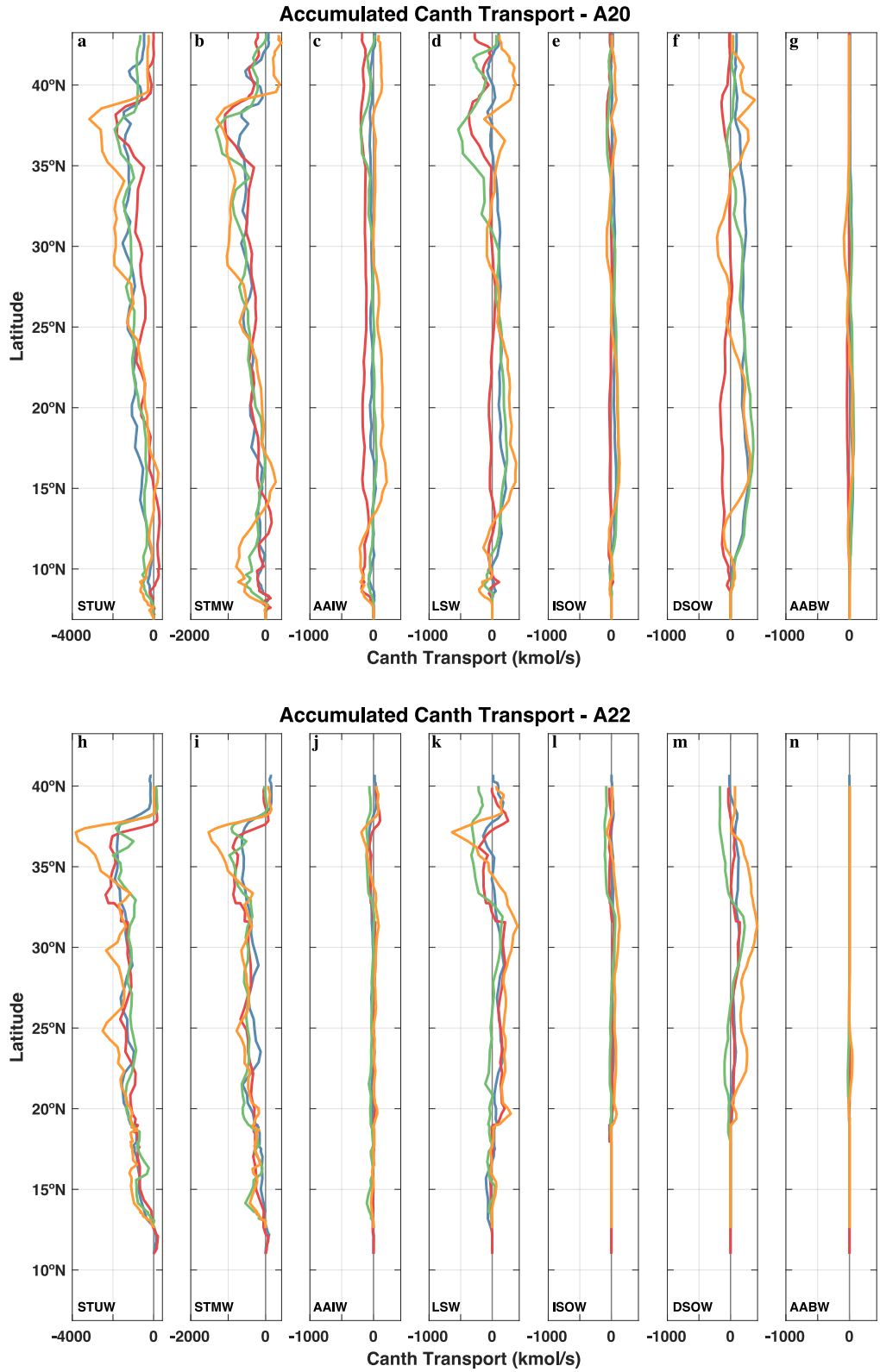

Figure 4. Northward accumulated C_{anth} transport (kmol/s) for each water mass, section, and surveyed year with colors corresponding to those in Figure 3. Panels (a–g) represent the A20 section (52°W) and panels (h–n) represent the A22 section (66°W). Water masses are arranged from the shallowest on the left to the deepest on the right. *X*-axis vary between subplots.

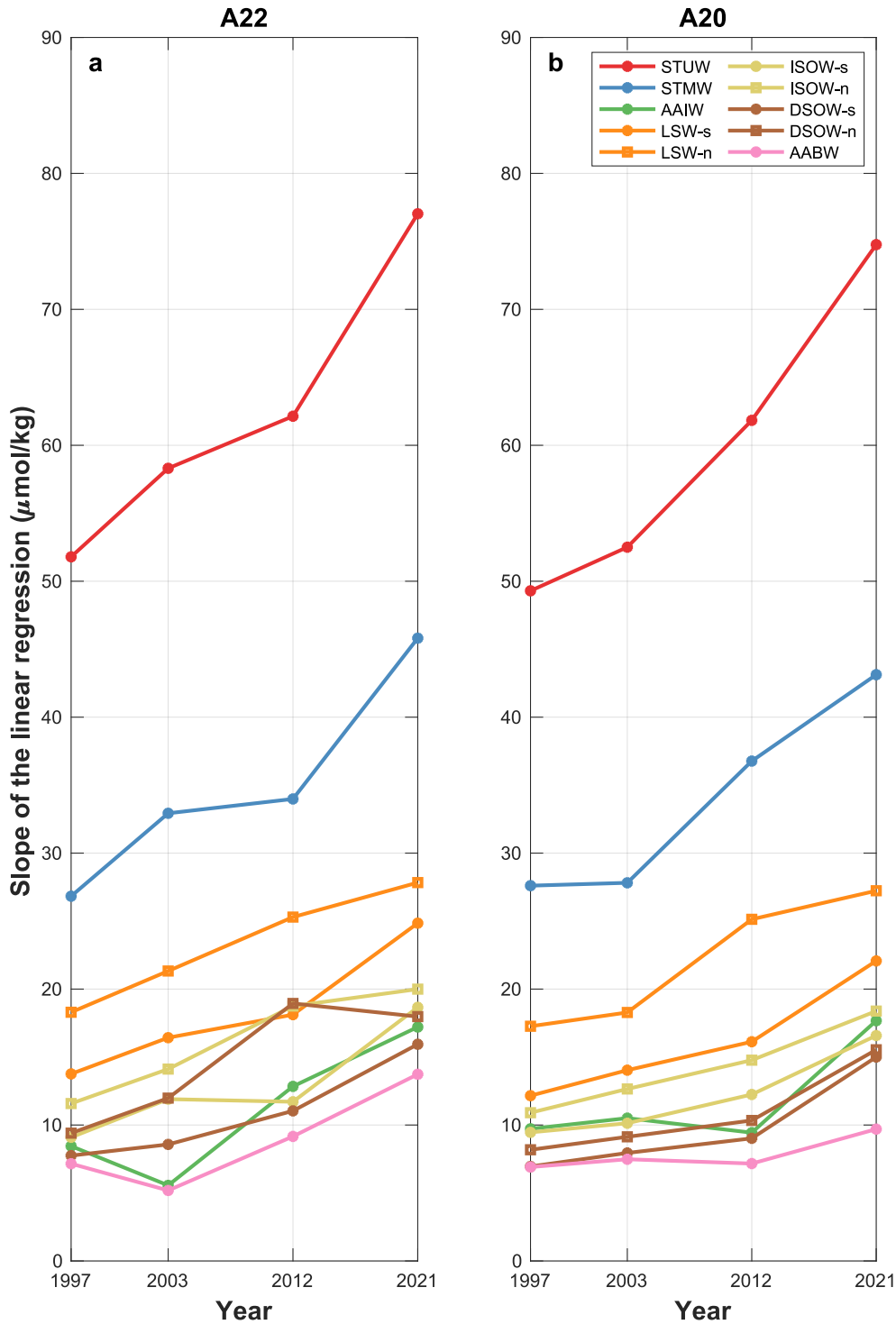

Figure 5. Slope of the linear correlation (μmol/kg) between C_{anth} transport (kmol/s) and mass transport (Sv) for each water mass over the surveyed years (1997, 2003, 2012, and 2021) in the A22 (a) and A20 (b) sections. The analysis separates water masses into northern (n) and southern (s) signals for deeper masses. The color scheme represents different water masses: STUW (red), STMW (blue), AAIW (green), Labrador Sea Water (orange), Iceland-Scotland Overflow Water (yellow), Denmark Strait Overflow Water (brown), and Antarctic Bottom Water (magenta).

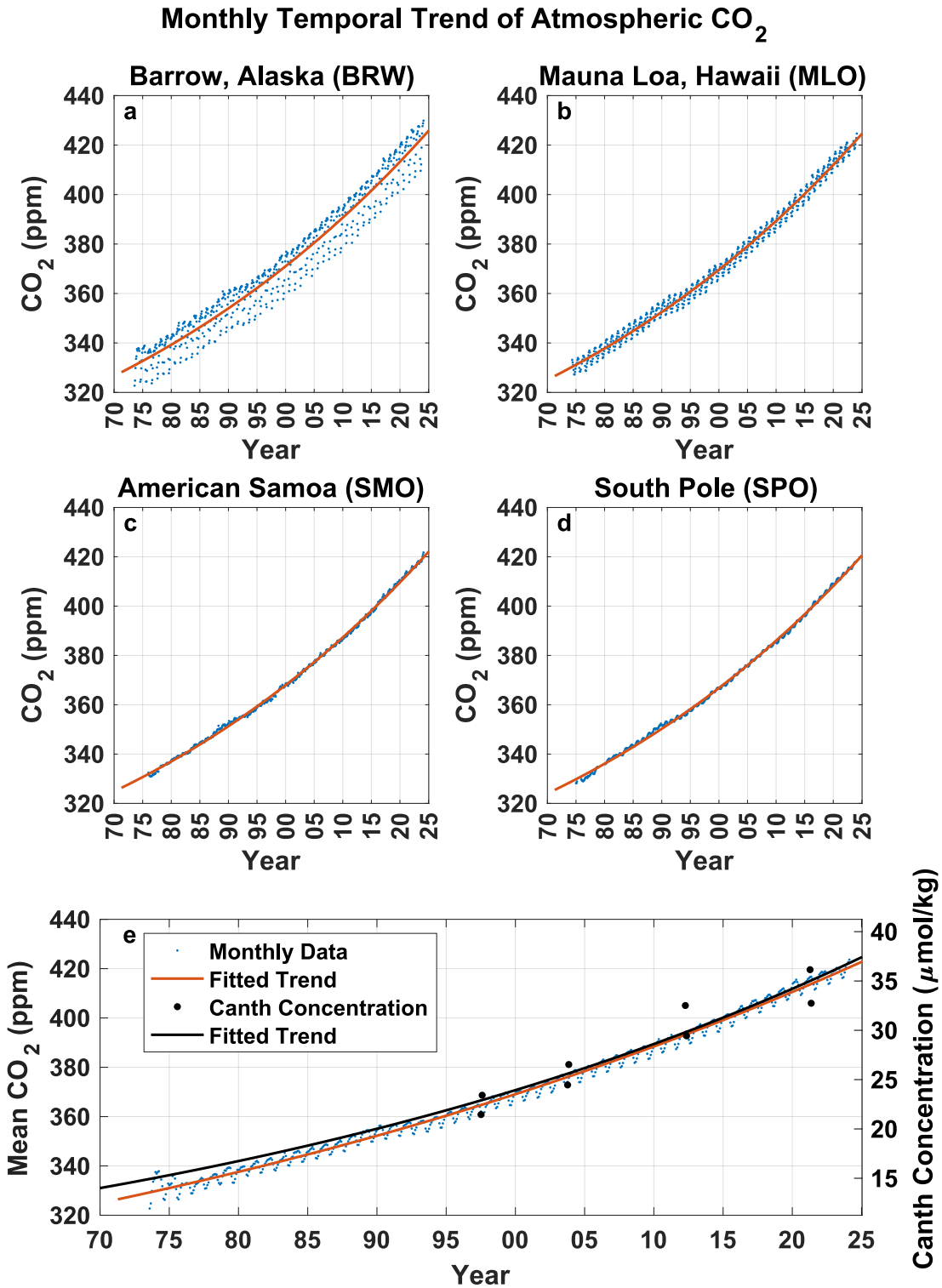

Figure 6. Temporal trends of atmospheric CO_2 concentrations (ppm) and oceanic C_{anth} concentrations (mol/kg) from 1970 to 2025. Panels (a–d) show the atmospheric CO_2 concentrations recorded at four monitoring stations: Barrow, Alaska (BRW; a), Mauna Loa, Hawaii (MLO; b), American Samoa (SMO; c), and the South Pole (SPO; d). Panel (e) displays the mean atmospheric CO_2 concentration derived from these stations (blue dots and red fitted trend) alongside the mean C_{anth} concentration from the A20 and A22 sections (black dots and black fitted trend).

diminished sensitivity arises from a reduced ocean buffering capacity combined with shifts in ocean circulation. These differences could arise from factors such as ocean circulation, temperature variability, and water mass dynamics, which influence the efficiency of CO_2 uptake in the region. The resemblance between atmospheric CO_2 and C_{anth} concentration trends implies that the western NASG is effectively capturing a portion of the increased atmospheric CO_2. Assessing whether regional CO_2 sequestration capacity keeps pace with rising atmospheric concentrations is therefore imperative. The four monitoring sites selected for this study provide critical insight within the global observational network. Moreover, the close correspondence between atmospheric CO_2 and C_{anth} trends suggests that the patterns observed in the NASG reflect broad global-scale processes rather than isolated regional phenomena.

4. Discussion

The findings of this study highlight the dominance of surface and intermediate layers in driving C_{anth} transport in the western NASG, particularly within the STUW and STMW layers. Similarly, Asselot et al. (2024) identify the upper subtropical waters and Subpolar Mode Water (SPMW) as key pathways for C_{anth} penetration, with vertical homogenization facilitated by winter convection. The consistent increasing trends in C_{anth} concentrations across surface layers reflect the strong linkage between air-sea CO_2 fluxes and oceanic uptake, as reported in Asselot et al. (2024) and the present study. However, the stratified nature of the subtropical NASG likely contributes to differences in the vertical mixing and storage efficiency of C_{anth} compared with the Subpolar North Atlantic (SPNA), where deeper winter convection allows for more pronounced C_{anth} penetration into intermediate and deep layers (Fröb et al., 2016; Steinfeldt et al., 2009). This work underscores the role of the GS and its recirculation in influencing C_{anth} transport patterns in the western NASG, particularly through its eastward flow in surface and intermediate layers. While the GS plays an important role in modulating C_{anth} distribution in the subtropical region, the North Atlantic Current (NAC) emerges as a critical link, carrying C_{anth}-rich waters from the subtropics into the SPNA. The NAC facilitates the transformation of these waters into SPMW and LSW through deep convection processes in the subpolar gyre (Asselot, Carracedo, et al., 2024; Pérez et al., 2008; Vázquez-Rodríguez et al., 2009). The variability of C_{anth} transport in deep layers, including the ISOW and DSOW, as observed in this study, aligns with Asselot et al.'s (2024) findings regarding the stepwise deepening of C_{anth} within the SPNA. However, while deep water formation and convection drive significant C_{anth} trapping in the SPNA, the weaker signals observed in the NASG may be attributed to the role of deep water mass circulating great distances from its origin regions until this region, in contrast to the SPNA as a source of C_{anth}. The episodic eastward and westward transport of DSOW observed here points to a more variable influence of deep boundary currents, in contrast to the consistently steady deep transport pathways documented in the SPNA (Asselot et al., 2024).

Bonou et al. (2024) documented consistent increases in CO_2 parameters, such as the partial pressure of CO_2 (pCO_2) and the total dissolved inorganic carbon in seawater (TCO_2), across the tropical Atlantic from 1985 to 2022, largely driven by rising atmospheric CO_2 levels. While their analysis highlights basin-wide trends, similar results (increasing in CO_2 concentration, C_{anth} concentration and also C_{anth} transport) presented here focus on the western NASG, therefore serving as validating part of the broader vision shown in their work. Bonou et al. (2024) attribute seasonal peaks in pCO_2 and TCO_2 to upwelling and biological activity, particularly during boreal spring and summer. Similarly, this study observes seasonal elevations in C_{anth} transport, but these are modulated latitudinally by the regional currents occurring and/or crossing the region (NBC, NEC, GS, DWBC).

Brown et al. (2021) explored the relationship between the AMOC and C_{anth} transport, emphasizing the impact of AMOC strength on northward transport. They found that a weakening AMOC reduced C_{anth} transport, which was partly mitigated by increasing surface C_{anth} concentrations. Similarly, this study highlights the predominant role of regional currents such as the GS and DWBC, which are branches of the AMOC, in shaping C_{anth} transport patterns in the western NASG. A notable aspect shared by both studies is the significant variability in C_{anth} transport. Brown et al. (2021) observed interannual fluctuations tied to AMOC variability while this study documents variations across surveyed years from the last 4 decades in the NASG. In both cases, surface and intermediate layers show the strongest transport trends. This reflects the sensitivity of C_{anth} transport to circulation dynamics and the pivotal role of upper-layer processes in redistributing C_{anth}-rich waters. Deep and bottom layers are addressed differently in the two studies but reveal complementary findings. Brown et al. (2021) emphasize the role of the AMOC's deep limb in transporting C_{anth} southward and facilitating its long-term sequestration in the

deep ocean. This aligns with the results of this study, where weaker C_{anth} transport signals in deeper water masses, such as LSW, ISOW, and DSOW, reflect limited concentrations and localized transport dynamics.

Ridge and McKinley (2020) noted that, although the North Atlantic has the highest per-area storage of C_{anth}, it was unclear whether the air–sea C_{anth} fluxes fueling that storage occur locally in the subpolar gyre or upstream in the subtropical gyre; by combining observations and an ocean hindcast model, they showed that air–sea uptake capacity is advected northward along the subsurface "nutrient stream," and that on the A22 section between Woods Hole and Bermuda these nutrient-stream waters are the oldest in the upper 2,000 m and relatively depleted in C_{anth}—yet still sufficient to sustain a subpolar uptake of ∼0.19 Pg C_{anth} yr^{-1}—and that despite some subtropical recirculation this pathway delivers uptake capacity into the subpolar gyre. Our repeated A22 occupations from 1997 to 2021 reproduce the same C_{anth} concentrations in the GS region (∼45 μmol kg^{-1} just below the mixed layer at 38°N; Figure 2), confirming that both tracer-injection and C* back-calculation methods isolate the nutrient-stream conveyor. Moreover, the time series of vertically integrated C_{anth} and atmospheric pCO_2 in the western subtropical gyre both increase exponentially over the study period (Figure 5), demonstrating that this uptake conveyor persists.

The results of this study can be contextualized alongside those of Pérez et al. (2018), which emphasize the role of the AMOC in the transport and storage of C_{anth} in the North Atlantic. In the NASG, this study identifies increasing trends in C_{anth} transport in surface and intermediate layers, primarily driven by rising atmospheric CO_2 concentrations and mediated by currents such as the GS and DWBC. Similarly, Pérez et al. (2018) demonstrate that the upper limb of the AMOC plays a critical role in delivering C_{anth} to the SPNA. Their findings show that AMOC-driven transport has led to a persistent increase in C_{anth} concentrations in SPMW and deeper layers, consistent with the upward trajectory observed in this study for northern regions. Another parallel lies in the recognition of the vertical distribution of C_{anth} concentration role -obeying the water masses' formation conditions- in modulating C_{anth} transport. This study finds weaker C_{anth} transport signals in deeper layers of the NASG, consistent with the lower concentrations observed in LSW, ISOW, and DSOW. Pérez et al. (2018) expand on this by linking the transport of acidified waters in the lower AMOC limb to significant shoaling of the Aragonite Saturation Horizon, which threatens cold-water coral ecosystems below this depth, the aragonite begins to dissolve rather than precipitate. Both studies highlight the vulnerability of deeper water masses to anthropogenic perturbations, though with a greater emphasis on ecological impacts in Pérez et al. (2018). Finally, both works address the interplay between C_{anth} transport and long-term changes in atmospheric CO_2. Pérez et al. (2018) estimate that doubling atmospheric CO_2 levels would severely exacerbate ocean acidification, reducing carbonate availability by up to 79% in preindustrial levels. This projection complements this study's findings, which suggest that rising C_{anth} concentrations are a major driver of increased transport across all water masses in the NASG.

In summary, rising C_{anth} concentrations in surface and intermediate layers have become the dominant force enhancing C_{anth} transport throughout the western NASG. Over the decades surveyed, temporal increases in C_{anth} concentrations have contributed more to the intensification of transport than changes in the strength or pathways of the water masses themselves. This highlights the primacy of concentration-driven mechanisms in governing oceanic carbon redistribution in the NASG.

Conflict of Interest

The authors declare no conflicts of interest relevant to this study.

Data Availability Statement

Hydrographic data were obtained from the https://cchdo.ucsd.edu/ as part of the International WOCE and GO-SHIP project databases. The data sets for the A20 cruises (1997, 2003, 2012, and 2021) are accessible at the following links: https://cchdo.ucsd.edu/cruise/316N151_3, https://cchdo.ucsd.edu/cruise/316N200309, https://cchdo.ucsd.edu/cruise/33AT20120419, and https://cchdo.ucsd.edu/cruise/325020210316. Similarly, the data sets for the A22 cruises (1997, 2003, 2012, and 2021) can be found here: https://cchdo.ucsd.edu/cruise/316N151_4, https://cchdo.ucsd.edu/cruise/316N200310, https://cchdo.ucsd.edu/cruise/33AT20120324, and https://cchdo.ucsd.edu/cruise/325020210420. Wind velocity data were sourced from the NCEP-DOE Reanalysis II project, provided by NOAA, and are available at https://psl.noaa.gov/data/gridded/data.ncep.reanalysis2.html.

Atmospheric CO_2 concentration data were retrieved from the NOAA GML CCGG database, accessible at https://gml.noaa.gov/ccgg/data/getdata.php?gas=co2. Matlab code for Canth estimation using the PHI-CT0 method is available for download at http://oceano.iim.csic.es/_media/cantphict0_toolbox_20190213.zip.

Acknowledgments

This research was conducted as part of the doctoral program in Oceanography and Global Change at IOCAG. The first author acknowledges the support of the "Ministerio de Universidades" through the Formación de Profesorado Universitario grant (FPU20/02211). The study was funded by the SAGA (RTI2018-100844-B-C31) and the SACO projects (PID2022-139403NB-C21) under the Ministerio de Ciencia, Innovación y Universidades of the Spanish Government. It is also a contribution from the Unidad Océano y Clima at Universidad de Las Palmas de Gran Canaria, an R&D&I CSIC-associated unit. The work forms part of the World Ocean Circulation Experiment (WOCE-WHP), the Climate Variability Hydrographic Program (CLIVAR), and the Global Ocean Ship-Based Hydrographic Investigations Program (GO-SHIP), funded by the National Science Foundation. We express our gratitude to the chief scientists responsible for collecting the A20 and A22 transect data: T. Joyce, W. Smethie, R. Curry, V. Menezes, R. Pickart, J. Toole, A. MacDonald, M. McCartney, and R. Woosley. Special thanks are extended to Adrián Vega Morales, hired through the INVESTIGO program for youth employment in research and innovation under the "Plan de Recuperación, Transformación y Resiliencia," funded by the European Union - NEXTGENERATIONEU.

References

Arumí-Planas, C., Pérez-Hernández, M. D., Pelegrí, J. L., Vélez-Belchí, P., Emelianov, M., Caínzos, V., et al. (2023). The South Atlantic circulation between 34.5°S, 24°S and above the Mid-Atlantic Ridge from an inverse box model. *Journal of Geophysical Research: Oceans*, *128*(5), e2022JC019614. https://doi.org/10.1029/2022JC019614

Asselot, R., Carracedo, L. I., Thierry, V., Mercier, H., Bajon, R., & Pérez, F. F. (2024). Anthropogenic carbon pathways towards the North Atlantic interior revealed by Argo-O_2, neural networks and back-calculations. *Nature Communications*, *15*(1), 1630. https://doi.org/10.1038/s41467-024-46074-5

Bonou, F., Dossa, A. N., Dahunsi, A. M., & Sohou, Z. (2024). Interannual and seasonal variability of CO_2 parameters in the tropical Atlantic Ocean. *Journal of Marine Science and Engineering*, *12*(12), 2248. https://doi.org/10.3390/jmse12122248

Brown, P. J., McDonagh, E. L., Sanders, R., Watson, A. J., Wanninkhof, R., King, B. A., et al. (2021). Circulation-driven variability of Atlantic anthropogenic carbon transports and uptake. *Nature Geoscience*, *14*(8), 571–577. https://doi.org/10.1038/s41561-021-00774-5

Caínzos, V., Pérez-Hernández, M. D., Santana-Toscano, D., Arumí-Planas, C., & Hernández-Guerra, A. (2023). Consistent picture of the horizontal circulation of the Atlantic Ocean over 3 decades. *Ocean Science*, *19*(4), 1009–1045. https://doi.org/10.5194/os-19-1009-2023

Caínzos, V., Velo, A., Pérez, F. F., & Hernández-Guerra, A. (2022). Anthropogenic carbon transport variability in the Atlantic Ocean over three decades. *Global Biogeochemical Cycles*, *36*(11), e2022GB007475. https://doi.org/10.1029/2022GB007475

Caldeira, K., & Wickett, M. E. (2003). Anthropogenic carbon and ocean pH. *Nature*, *425*(6956), 365. https://doi.org/10.1038/425365a

Caldeira, K., & Wickett, M. E. (2005). Ocean model predictions of chemistry changes from carbon dioxide emissions to the atmosphere and ocean. *Journal of Geophysical Research*, *110*(C9), 1–12. https://doi.org/10.1029/2004JC002671

Casanova-Masjoan, M., Joyce, T. M., Pérez-Hernández, M. D., Vélez-Belchí, P., & Hernández-Guerra, A. (2018). Changes across 66°W, the Caribbean Sea and the Western boundaries of the North Atlantic Subtropical Gyre. *Progress in Oceanography*, *168*, 296–309. https://doi.org/10.1016/j.pocean.2018.09.013

Comas-Rodríguez, I., Hernández-Guerra, A., & McDonagh, E. L. (2010). Referencing geostrophic velocities using ADCP data. *Scientia Marina*, *74*(2), 331–338. https://doi.org/10.3989/scimar.2010.74n2331

Curbelo-Hernández, D., Pérez, F. F., González-Dávila, M., Gladyshev, S. V., González, A. G., González-Santana, D., et al. (2024). Ocean acidification trends and carbonate system dynamics in the North Atlantic subpolar gyre during 2009–2019. *EGUsphere*. https://doi.org/10.5194/egusphere-2024-1388

Cushman-Roisin, B., & Beckers, J. M. (1994). *Introduction to Geophysical Fluid Dynamics* (1st ed.). Pearson College Div (Prentice-Hall imprint).

Doney, S. C., Busch, D. S., Cooley, S. R., & Kroeker, K. J. (2020). The impacts of ocean acidification on marine ecosystems and reliant human communities. *Annual Review of Environment and Resources*, *45*(1), 83–112. https://doi.org/10.1146/ANNUREV-ENVIRON-012320-083019

Doney, S. C., Fabry, V. J., Feely, R. A., & Kleypas, J. A. (2009). Ocean acidification: The other CO_2 problem. *Annual Review of Marine Science*, *1*(1), 169–192. https://doi.org/10.1146/annurev.marine.010908.163834

Feely, R. A., Sabine, C. L., Lee, K., Berelson, W., Kleypas, J., Fabry, V. J., & Millero, F. J. (2004). Impact of anthropogenic CO_2 on the $CaCO_3$ system in the oceans. *Science*, *305*(5682), 362–366. https://doi.org/10.1126/SCIENCE.1097329

Friedlingstein, P., O'Sullivan, M., Jones, M. W., Andrew, R. M., Bakker, D. C. E., Hauck, J., et al. (2023). Global carbon budget 2023. *Earth System Science Data*, *15*(12), 5301–5369. https://doi.org/10.5194/essd-15-5301-2023

Fröb, F., Olsen, A., Våge, K., Moore, G. W. K., Yashayaev, I., Jeansson, E., & Rajasakaren, B. (2016). Irminger Sea deep convection injects oxygen and anthropogenic carbon to the ocean interior. *Nature Communications*, *7*(1), 13244. https://doi.org/10.1038/ncomms13244

Ganachaud, A., & Wunsch, C. (2000). Improved estimates of global ocean circulation, heat transport and mixing from hydrographic data. *Nature*, *408*(6811), 453–457. https://doi.org/10.1038/35044048

García-Ibáñez, M. I., Zunino, P., Fröb, F., Carracedo, L. I., Ríos, A. F., Mercier, H., et al. (2016). Ocean acidification in the subpolar North Atlantic: Rates and mechanisms controlling pH changes. *Biogeosciences*, *13*(12), 3701–3715. https://doi.org/10.5194/BG-13-3701-2016

Gattuso, J. P., Magnan, A., Billé, R., Cheung, W. W. L., Howes, E. L., Joos, F., et al. (2015). Contrasting futures for ocean and society from different anthropogenic CO_2 emissions scenarios. *Science*, *349*(6243), aac4722. https://doi.org/10.1126/SCIENCE.AAC4722

Gruber, N., Clement, D., Carter, B. R., Feely, R. A., van Heuven, S., Hoppema, M., et al. (2019). The oceanic sink for anthropogenic CO_2 from 1994 to 2007. *Science*, *363*(6432), 1193–1199. https://doi.org/10.1126/SCIENCE.AAU5153

Gruber, N., Sarmiento, J. L., & Stocker, T. F. (1996). An improved method for detecting anthropogenic CO_2 in the oceans. *Global Biogeochemical Cycles*, *10*(4), 809–837. https://doi.org/10.1029/96GB01608

Guinotte, J. M., Orr, J., Cairns, S. D., Freiwald, A., Morgan, L., & George, R. (2006). Will human-induced changes in seawater chemistry alter the distribution of deep-sea scleractinian corals? *Frontiers in Ecology and the Environment*, *4*(3), 141–146. https://doi.org/10.1890/1540-9295(2006)004

Hall, M. M., Joyce, T. M., Pickart, R. S., Smethie, W. M., Jr., & Torres, D. J. (2004). Zonal circulation across 52°W in the North Atlantic. *Journal of Geophysical Research*, *109*(C11), C11008. https://doi.org/10.1029/2003JC002103

Hernández-Guerra, A., Talley, L. D., Pelegrí, J. L., Vélez-Belchí, P., Baringer, M. O., Macdonald, A. M., & McDonagh, E. L. (2019). The upper, deep, abyssal and overturning circulation in the Atlantic Ocean at 30°S in 2003 and 2011. *Progress in Oceanography*, *176*, 102136. https://doi.org/10.1016/j.pocean.2019.102136

Jackett, D. R., & McDougall, T. J. (1997). A neutral density variable for the world's oceans. *Journal of Physical Oceanography*, *27*(2), 237–263. https://doi.org/10.1175/1520-0485(1997)027<0237:ANDVFT>2.0.CO;2

Joyce, T. M., Hernandez-Guerra, A., & Smethie, W. M. (2001). Zonal circulation in the NW Atlantic and Caribbean from a meridional World Ocean Circulation Experiment hydrographic section at 66°W. *Journal of Geophysical Research*, *106*(C10), 22095–22113. https://doi.org/10.1029/2000JC000268

Kanamitsu, M., Ebisuzaki, W., Woollen, J., Yang, S.-K., Hnilo, J. J., Fiorino, M., & Potter, G. L. (2002). NCEP–DOE AMIP-II Reanalysis (R-2). *Bulletin of the American Meteorological Society*, *83*(11), 1631–1644. https://doi.org/10.1175/BAMS-83-11-1631

Khatiwala, S., Primeau, F., & Hall, T. (2009). Reconstruction of the history of anthropogenic CO_2 concentrations in the ocean. *Nature*, *462*(7271), 346–349. https://doi.org/10.1038/nature08526

Khatiwala, S., Tanhua, T., Mikaloff Fletcher, S., Gerber, M., Doney, S. C., Graven, H. D., et al. (2013). Global ocean storage of anthropogenic carbon. *Biogeosciences*, *10*(4), 2169–2191. https://doi.org/10.5194/bg-10-2169-2013

Li, X., Wu, Z., Ouyang, Z., & Cai, W.-J. (2024). The source and accumulation of anthropogenic carbon in the U.S. East Coast. *Science Advances*, *10*(32), eadl3169. https://doi.org/10.1126/sciadv.adl3169

Matear, R. J., Wong, C. S., & Xie, L. (2003). Can CFCs be used to determine anthropogenic CO_2? *Global Biogeochemical Cycles*, *17*(1), 1013. https://doi.org/10.1029/2001GB001415

Müller, J. D., Gruber, N., Carter, B., Feely, R., Ishii, M., Lange, N., et al. (2023). Decadal trends in the oceanic storage of anthropogenic carbon from 1994 to 2014. *AGU Advances*, *4*(4). https://doi.org/10.1029/2023av000875

Orr, J. C., Fabry, V. J., Aumont, O., Bopp, L., Doney, S. C., Feely, R. A., et al. (2005). Anthropogenic ocean acidification over the twenty-first century and its impact on calcifying organisms. *Nature*, *437*(7059), 681–686. https://doi.org/10.1038/nature04095

Pérez, F. F., Fontela, M., García-Ibáñez, M. I., Mercier, H., Velo, A., Lherminier, P., et al. (2018). Meridional overturning circulation conveys fast acidification to the deep Atlantic Ocean. *Nature*, *554*(7693), 515–518. https://doi.org/10.1038/nature25493

Pérez, F. F., Mercier, H., Vázquez-Rodríguez, M., Lherminier, P., Velo, A., Pardo, P. C., et al. (2013). Atlantic Ocean CO_2 uptake reduced by weakening of the meridional overturning circulation. *Nature Geoscience*, *6*(2), 146–152. https://doi.org/10.1038/ngeo1680

Pérez, F. F., Vázquez-Rodríguez, M., Louarn, E., Padín, X. A., Mercier, H., & Ríos, A. F. (2008). Temporal variability of the anthropogenic CO_2 storage in the Irminger Sea. *Biogeosciences*, *5*(6), 1669–1679. https://doi.org/10.5194/bg-5-1669-2008

Pérez, F. F., Vázquez-Rodríguez, M., Mercier, H., Velo, A., Lherminier, P., & Ríos, A. F. (2010). Trends of anthropogenic CO_2 storage in North Atlantic water masses. *Biogeosciences*, *7*(5), 1789–1807. https://doi.org/10.5194/bg-7-1789-2010

Raven, J., Caldeira, K., Elderfield, H., Hoegh-Guldberg, O., Liss, P., Riebesell, U., et al. (2005). *Ocean acidification due to increasing atmospheric carbon dioxide* (p. 60). The Royal Society. Retrieved from https://royalsociety.org/topics-policy/publications/2005/ocean-acidification/

Ridge, S. M., & McKinley, G. A. (2020). Advective controls on the north Atlantic anthropogenic carbon sink. *Global Biogeochemical Cycles*, *34*(7). https://doi.org/10.1029/2019gb006457

Sabine, C. L., Feely, R. A., Gruber, N., Key, R. M., Lee, K., Bullister, J. L., et al. (2004). The oceanic sink for anthropogenic CO_2. *Science*, *305*(5682), 367–371. https://doi.org/10.1126/SCIENCE.1097403

Santana-Toscano, D., Pérez-Hernández, M. D., Arumí-Planas, C., & Hernández-Guerra, A. (2025). Estimating the western North Atlantic Subtropical Gyre zonal currents in 2021 through single- and three-box inverse models. *Progress in Oceanography*, *231*, 103415. https://doi.org/10.1016/J.POCEAN.2025.103415

Santana-Toscano, D., Pérez-Hernández, M. D., Macdonald, A. M., Arumí-Planas, C., Caínzos, V., & Hernández-Guerra, A. (2023). Zonal circulation in the North Atlantic ocean at 52°W from WOCE-WHP and CLIVAR sections: 1997, 2003 and 2012. *Progress in Oceanography*, *216*, 103069. https://doi.org/10.1016/J.POCEAN.2023.103069

Steinfeldt, R., Rhein, M., Bullister, J. L., & Tanhua, T. (2009). Inventory changes in anthropogenic carbon from 1997–2003 in the Atlantic Ocean between 20°S and 65°N. *Global Biogeochemical Cycles*, *23*(3), GB3010. https://doi.org/10.1029/2008GB003311

Talley, L. D., Feely, R. A., Sloyan, B. M., Wanninkhof, R., Baringer, M. O., Bullister, J. L., et al. (2016). Changes in ocean heat, carbon content, and ventilation: A review of the first decade of GO-SHIP global repeat hydrography. *Annual Review of Marine Science*, *8*(1), 185–215. https://doi.org/10.1146/annurev-marine-052915-100829

Thomas, H., & Ittekkot, V. (2001). Determination of anthropogenic CO_2 in the North Atlantic Ocean using water mass ages and CO_2 equilibrium chemistry. *Journal of Marine Systems*, *27*(4), 325–336. https://doi.org/10.1016/S0924-7963(00)00077-4

Thoning, K. W., Crotwell, A. M., & Mund, J. W. (2024). *Atmospheric carbon dioxide dry air mole fractions from continuous measurements at Mauna Loa, Hawaii, Barrow, Alaska, American Samoa and South Pole, 1973–present*. Global Monitoring Laboratory (GML). https://doi.org/10.15138/YAF1-BK21

Touratier, F., Azouzi, L., & Goyet, C. (2007). CFC-11, $\Delta^{14}C$ and ^{3}H tracers as a means to assess anthropogenic CO_2 concentrations in the ocean. *Tellus B*, *59*(2), 318–325. https://doi.org/10.1111/j.1600-0889.2006.00247.x

Vázquez-Rodríguez, M., Touratier, F., Lo Monaco, C., Waugh, D. W., Padin, X. A., Bellerby, R. G. J., et al. (2009). Anthropogenic carbon distributions in the Atlantic Ocean: Data-based estimates from the Arctic to the Antarctic. *Biogeosciences*, *6*(3), 439–451. https://doi.org/10.5194/bg-6-439-2009

Waugh, D. W., Hall, T. M., McNeil, B. I., Key, R., & Matear, R. J. (2006). Anthropogenic CO_2 in the oceans estimated using transit time distributions. *Tellus B: Chemical and Physical Meteorology*, *58*(5), 376. https://doi.org/10.1111/j.1600-0889.2006.00222.x

Wunsch, C. (1978). The North Atlantic general circulation west of 50°W determined by inverse methods. *Reviews of Geophysics*, *16*(4), 583–620. https://doi.org/10.1029/RG016i004p00583

Wunsch, C. (1996). The steady ocean circulation inverse problem. In *The Ocean Circulation Inverse Problem* (pp. 212–296). Cambridge University Press. https://doi.org/10.1017/CBO9780511629570.006